International Journal of Advanced Mathematical Sciences, 12 (1) (2026) 68-78

International Journal of Advanced Mathematical Sciences

Website: www.sciencepubco.com/index.php/IJAMS
https://doi.org/10.14419/4bv4wg35
Research paper

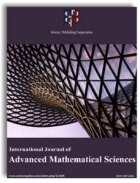

Elastico–Viscous Boundary Layer Flow Over A Wedge Incorporating Nanofluid Interaction Effects

Bikash Koli Saha *

Independent Researcher, Mathematics, Guwahati, Kamrup Metropolitan, Assam, Pin:781018, India
**Corresponding author E-mail: bikashkoli100@gmail.com*

Abstract

The present discourse delineates a rigorous examination of steady elastico–viscous boundary layer flow past a wedge embedded within a nanofluid environment under a uniform free-stream velocity. The framework imposes isothermal boundary conditions alongside a prescribed homogeneous quantifiable measure of nanoparticle occupancy relative to the total fluidic domain at the stretching interface. The governing relations for the coupled mechanisms of momentum transfer, thermo-energetic diffusion, and nanoparticle volumetric stratification are constructed via Walter's liquid model B/ synergistically coupled with the Kuznetsov–Nield nanofluid formulation [27-28]. Through the application of similarity transformations, augmented by appropriate boundary constraints, the system is reformulated as a nonlinear system of ordinary differential relations, subsequently addressed via the bvp4c numerical integrator embedded within MATLAB. The outcomes underscore the decisive role of the elastico–viscous parameter in modulating velocity, thermal, and concentration distributions, while simultaneously elucidating the coupled dynamics of the conjoint modulation of hydrodynamic, thermo-diffusive, and concentration stratified layers in shaping the overall transport phenomena of the system.

Keywords: *Boundary Layer; Elastico-Viscous Fluid; Nanofluid; Shrinking Wedge; Stretching Wedge.*

1. Introduction

To exemplify the applicability of Prandtl's boundary layer framework, Falkner and Skan [1] pioneered the analysis of continuous laminar flow past a stationary wedge. Within the evolving corpus of nanofluid investigations, Saidur et al. [2] synthesized an extensive review delineating diverse commercial, residential, industrial, and transportation-related utilizations. Complementarily, Mahian et al. [3] and Behar et al. [4] provided critical expositions of contemporary advancements in nanofluid-based heat transfer phenomena, whereas Bondareva et al. [5] specifically explored alumina–water nanofluid systems. Saidur et al. [6] further consolidated the discourse through a comprehensive examination of nanofluid technologies. Monographs [7–10] and review treatises [11–17] constitute significant repositories encompassing theoretical and empirical inquiries into nanofluid genesis, rheological traits (e.g., viscosity and thermal conductivity), and convective transport dynamics. Moreover, the emergent paradigm of hybrid nanofluids, as introduced by Sheikholeslami et al. [18], underscores a nascent trajectory of innovation.

The mechanism of mitigating interfacial resistance between two contacting or mating surfaces when they roll against one another is referred to in this context as lubrication. The protective layer of nanoparticles found in nano-lubrication is present between surfaces that come into contact with one another, improving performance and efficiency. Taking into account the aforementioned considerations, the metal-cutting machining operation employs nano-lubrication to enhance tribological performance and thermal management at the tool–workpiece interface. Nano-lubrication is the method of using a nanofluid as a cutting fluid to effectively cool and lubricate the cutting zone (metal working zone) during any machining operation.

Metal cutting is the process of using a wedge-shaped tool to remove excess material from a workpiece in the shape of a chip. This process maintains the focus on several factors that affect the manufacturing class, including the tool's durability, the work surface's probity, the amount of material detached, the amount of heat generated when a workpiece comes into contact with a tool, and specific energy expenditure [19-21]. By using CNC-CuO Nano lubricant in internal combustion engines, Hisham et al. [22] improved its stability for a sustainable environment. The stability of the entire system was assessed using zeta potential tests.

Furthermore, in order to determine the friction coefficient and wear rate, fluid lubrication was employed in circumstances with the rapid kinematic escalation concomitant with minimal external resistance, and boundary lubrication was employed in circumstances with low acceleration and high load. In conjunction with SAE 40 base oil, nanolubricant formulations incorporating nanoparticle concentrations within the interval 0.1%–0.9% were systematically investigated. Zeta potential diagnostics revealed an enhancement in colloidal stability up to the 0.5% threshold, beyond which a decline was observed at 0.9%. The CNC–CuO nanolubricants exhibited pronounced tribological superiority, manifesting as substantial attenuation of the friction coefficient—quantified as reductions of approximately 33%–44% under blended lubrication regimes and 48%–50% under boundary lubrication conditions.

Zawawi et al. [23] conducted an experimental inquiry employing TiO_2/SiO_2 polyol-ester–based nanolubricants within automotive electrical compressor air-conditioning systems, with volumetric concentrations spanning 0.01%–1%. At an optimal concentration of 0.03%, the

Copyright © Bikash Koli Saha. This is an open access article distributed under the Creative Commons Attribution License, which permits unrestricted use, distribution, and reproduction in any medium, provided the original work is properly cited.

nanolubricant augmented thermal absorption by as much as 44.2%. In a related vein, Khan and Pop [24] examined boundary layer transport phenomena over a wedge translating through a nanofluid medium, wherein the adopted thermal dispersion construct exhibits strong correspondence with the formulations advanced by Nield and Kuznetsov [25] and subsequently refined by Kuznetsov and Nield [26].

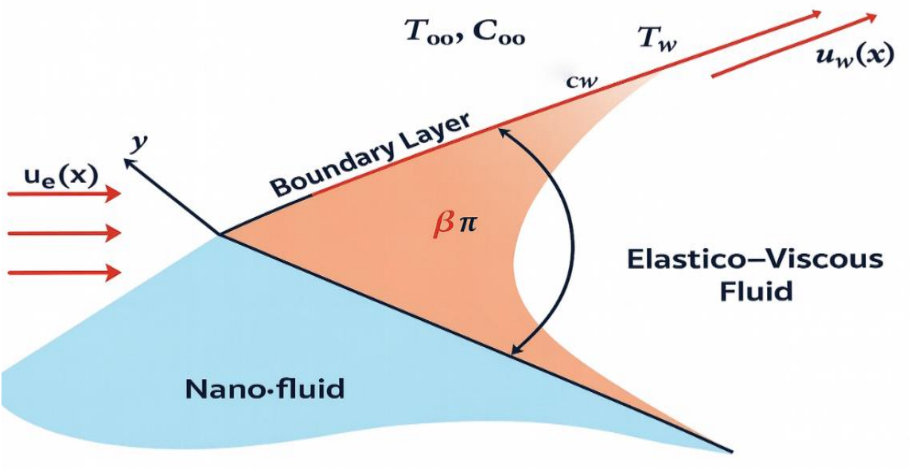

Fig. 1.1: Flow Configuration.

In light of this, it is important to emphasize that nanotechnology has been applied extensively in the industry, attributable to the distinctive physicochemical attributes inherent in materials with nanometers.

2. Mathematical Formulation

The present discourse is devoted to the analytical exploration of elastico-viscous boundary-layer phenomena engendered by an impermeable wedge subject to stretching dynamics within a Nano fluidic environment. The kinematic prescription at the solid boundary is characterized by a stream-wise-dependent surface velocity, $u_w(x)$, counterpoised with an external inviscid flow velocity field, $u_e(x)$, wherein the spatial coordinate x signifies the longitudinal abscissa traced along the wedge contour, as schematically represented in Figure 1. The parametric sign of $u_w(x)$ delineates the morphokinematic regime, with $u_w(x) > 0$ corresponding to wedge elongation (stretching) and $u_w(x) < 0$ to wedge contraction. Thermo-physical boundary stipulations impose invariant wall conditions for temperature. T_w and nanoparticle concentration C_w, whereas the far-field asymptotic enforces convergence toward the ambient states T_∞ and C_∞ as $y \to \infty$.
Subject to these constitutive and asymptotic constraints, the governing quasi-parabolic framework of steady-state boundary-layer governing relations—encompassing the continuity condition, the elastico–viscous momentum transport equation, the thermal energy diffusion relation, and the nanoparticle species conservation law—are articulated in the Cartesian coordinate framework (x, y), consistent with the foundational formulations advanced by Nield and Kuznetsov [25] and later extended through the refinements introduced by Kuznetsov and Nield [26].

$$\frac{\partial u}{\partial x}+\frac{\partial v}{\partial y}=0 \tag{2.1}$$

$$u\frac{\partial u}{\partial x}+v\,\frac{\partial u}{\partial y}=u_e(x)\frac{du_e}{dx}+\nu\frac{\partial^2 u}{\partial y^2}-\frac{k_0}{\rho}\left[u\frac{\partial^3 u}{\partial x\,\partial y^2}+v\frac{\partial^3 u}{\partial y^3}-\frac{\partial u}{\partial y}\frac{\partial^2 u}{\partial x\,\partial y}-\frac{\partial v}{\partial y}\frac{\partial^2 u}{\partial y^2}\right] \tag{2.2}$$

$$u\frac{\partial T}{\partial x}+v\,\frac{\partial T}{\partial y}=\alpha\frac{\partial^2 T}{\partial y^2}+\tau\left[D_B\,\frac{\partial C}{\partial y}\,\frac{\partial T}{\partial y}+\left(\frac{D_T}{D_\infty}\right)\left(\frac{\partial T}{\partial y}\right)^2\right] \tag{2.3}$$

$$u\frac{\partial C}{\partial x}+v\,\frac{\partial C}{\partial y}=D_B\frac{\partial^2 C}{\partial y^2}+\left(\frac{D_T}{D_\infty}\right)\frac{\partial^2 T}{\partial y^2} \tag{2.4}$$

Consistent with the enforcement of the designated boundary stipulations [24]

$$v=0,\ u=u_w(x)=-\lambda\,u_e(x)\,,\ T=T_w\,,\ C=C_w \text{ at } y\to 0 \tag{2.5}$$

$$u=u_e(x),\ T=T_\infty,\ C=C_\infty \text{ at } y\to\infty \tag{2.6}$$

The hydrodynamic field is characterized by the Cartesian-resolved velocity fields. u and v defining the flow kinematics, respectively, along the streamwise (x) and transverse (y). The material response incorporates the elastico-viscous parameter. k_0 , while **υ** denotes the kinematic viscosity and α the thermal diffusivity of the carrier medium. Nanoparticle transport phenomena are parameterized through the Brownian diffusion coefficient. D_B and the thermophoresis diffusion coefficient D_T. The effective heat capacity ratio is expressed as $\tau = \frac{(\rho c)_\rho}{(\rho c)_f}$, with ρ symbolizing the fluid density, c the volumetric heat capacity, and ρ_p the intrinsic density of the dispersed particulate phase.
The foundational framework of differential relations governing the flow (2.1) – (2.6) is rendered amenable to analytical treatment via the invocation of an appropriate similarity transformation, wherein the functional dependencies of the wedge surface velocity are considered. $u_w(x)$ and the external free-stream velocity $u_e(x)$ are prescribed in the ensuing canonical form.
The surface-driven kinematic prescription is parameterized as $u_w(x) = ax^m$, while the corresponding external free-stream velocity distribution is analogously represented by $u_e(x) = cx^m$, wherein the constants a and c serve as scaling coefficients and the exponent m embodies the wedge-induced similarity index governing the stream-wise acceleration field [24]:

$$u_w(x) = ax^m \text{ and } u_e(x) = cx^m \tag{2.7}$$

Let a, c and m be non-negative constants subject to the constraint $0 \leq m \leq 1$. The kinematic motion parameter is introduced as $\lambda = \frac{c}{a}$, wherein the regimes $\lambda < 0, \lambda > 0$ and $\lambda = 0$ respectively characterize a stretching wedge, a contracting (shrinking) wedge, and a stationary wedge configuration. Invoking the boundary prescriptions (2.5) – (2.6), a self-similar reduction of the governing system (2.1) – (2.4) is pursued to secure an invariant similarity solution [24]:

$$\boldsymbol{\psi} = (\frac{2u_e x\nu}{1+m})^{\frac{1}{2}} f(\zeta),\ \theta(\zeta) = \frac{T - T_\infty}{T_w - T_\infty},\ \boldsymbol{\phi}(\zeta) = \frac{C - C_\infty}{C_w - C_\infty},\ \zeta = \{\frac{(1+m)u_e}{2x\upsilon}\}^{\frac{1}{2}} y,\ u = \frac{\partial\psi}{\partial y},\ v = -\frac{\partial\psi}{\partial x} \tag{2.8}$$

In this formulation, $\boldsymbol{\psi}$ and ζ denote the stream function and the similarity variable, respectively. Upon the substitution of relation (2.8) into the governing system (2.1) – (2.4), the equations reduce to their corresponding autonomous ordinary differential forms.

$$f'''(\zeta) + f(\zeta)f''(\zeta) + \beta[1 - \{f'(\zeta)\}^2] - k_1\left[2f'(\zeta)f'''\zeta) - \{f''(\zeta)\}^2 - Af(\zeta)f^{iv}(\zeta)\right] = 0 \tag{2.9}$$

$$\frac{1}{p_r}\theta''(\zeta) + f(\zeta)\,\theta'(\zeta) + N_b\phi'(\zeta)\theta'(\zeta) + N_t\theta'(\zeta)\}^2 = 0 \tag{2.10}$$

$$\phi''(\zeta) + \text{Le}\, f(\zeta)\phi'(\zeta) + \frac{N_t}{N_b}\theta''(\zeta) = 0 \tag{2.11}$$

With reference to the imposed boundary constraints

$$f(0) = 0,\ f'(0) = -\lambda,\ \theta(0) = 1,\ \phi(0) = 1 \text{ as } \zeta \to 0 \tag{2.12}$$

$$f'(\infty) = 1,\ \theta(\infty) = 0,\ \phi(\infty) = 0 \text{ as } \zeta \to \infty \tag{2.13}$$

Here, the prime notation signifies differentiation relative to the similarity transformed. ζ, and the dynamical framework is governed by seven dimensionless control parameters, delineated as follows:

$$\beta = \frac{2m}{1+m},\ k_1 = \frac{k_0}{\rho}\frac{u_e{}^3(1+m)}{4x^2\upsilon},\ \text{A} = \frac{1+m}{3m-1} = \frac{1}{2\beta - 1},\ \text{Pr} = \frac{\upsilon}{\alpha},\ \text{Le} = \frac{\upsilon}{D_B},\ N_b = \frac{(\rho c)_p D_B(\phi_w - \phi_\infty)}{(\rho c)_f \upsilon},$$

$$N_t = \frac{(\rho c)_p D_T(T_w - T_\infty)}{(\rho c)_f T_\infty \upsilon} \tag{2.14}$$

The pressure gradient, the modified elastico-viscous parameter associated with it, the pressure-gradient–related parameter, the Prandtl and Lewis numbers, along with the stochastic nanoparticle transport induced by Brownian agitation and the thermally driven migratory flux arising from thermophoresis forces, are quantified by $\beta, k_1, A, Pr, Le, N_b, and\ N_t$ respectively. Notably, setting $\lambda = 0, N_b = 0\ and\ N_t = 0$. (2.10) – (2.11) reduces the formulation to the classical Falkner–Skan [1] boundary-layer problem for a hydro-dynamically viscous, incompressible continuum flow field interacting with a quiescent wedge-shaped geometry.

3. Solution Scheme

The self-similar nonlinear differential relations (2.9) – (2.11) are recast into an equivalent canonical representation comprising a linked ensemble of first-order ordinary differential constructs:

$$f = y_1, f' = y_2,\ f'' = y_3, f''' = y_4, \theta = y_5, \theta' = y_6, \phi = y_7, \phi' = y_8 \tag{3.1}$$

(3.1) enables the formulation of

$$y_1' = y_2, y_2' = y_3, y_3' = y_4, y_5' = y_6, y_7' = y_8 \tag{3.2}$$

Equations (2.9), (2.10), and (2.11) may be reformulated in terms of (3.1) and (3.2) as given below:

$$y_4{}' = -\frac{(3m-1)}{(1+m)y_1}\left[(y_3^2 - 2y_2y_4) + \frac{1}{k_1}\{y_4 + y_1y_3 + \frac{2m}{1+m}(1 - y_2{}^2\}\right] \tag{3.3}$$

$$y_4{}' = -\frac{2\beta - 1}{y_1}\left[(y_3^2 - 2y_2y_4) + \frac{1}{k_1}\{y_4 + y_1y_3 + \beta(1 - y_2{}^2)\}\right] \tag{3.4}$$

$$y_6' = -Pr(y_1y_6 + N_by_8y_6 + N_ty_6{}^2) \tag{3.5}$$

$$y_8' = -(\text{Le}y_1y_8 + \frac{N_t}{N_b}y_6') \tag{3.6}$$

And the following are the reduction of the pertinent boundary conditions (2.12) and (2.13):

$$y_1(0) = 0,\ y_2(0) = -\lambda,\ y_5(0) = 1,\ y_7(0) = 1 \tag{3.7}$$

$$y_2(\infty) = 1,\ y_3(\infty) = 0,\ y_5(\infty) = 0,\ y_7(\infty) = 0 \tag{3.8}$$

MATLAB’s bvp4c algorithm for the numerical treatment of boundary-value differential systems is utilized to obtain numerical realizations of equations (3.3), (3.5), and (3.6), constrained by boundary prescriptions (3.7) – (3.8), across a spectrum of flow-governing parameter regimes.

4. Results and Discussion

The MATLAB intrinsic boundary-value solver bvp4c is invoked to compute the stratified distributions of momentum, thermal energy, and nano-particle concentration, thereby elucidating the dynamical implications of the governing similarity parameters. The parametric sensitivities of the flow fields are exhibited in Figures 4.2–4.17. To establish the credibility of the formulation, the numerically obtained quantities—namely, the surface shear stress induced by viscous effects $f''(0)$ as well as the thermal gradient at the bounding surface$-\theta'(0)$ are systematically benchmarked against reference data from the literature, with the comparative results (Tables 4.1–4.2) demonstrating close concordance.

Table 4.1 furnishes a comparative assessment of the computed values of $f''(0)$ with those reported in equation (3.3) for different m under the condition $k_1 = \lambda = 0$. Similarly, Table 4.2 contrasts the surface temperature gradients $-\theta'(0)$, computed from equations (3.3) and (3.5) for $m = 0$ and varying Pr, with benchmark results from (3.3) and (3.5), assuming $\lambda = N_b = N_t = 0$ [32,33]. The close agreement observed across these comparisons substantiates both the correctness and the high precision of the present numerical findings.

Table 4.1: The Tabulated Magnitudes of $f''(0)$ Are Delineated Across A Spectrum of the Wedge-Geometry Index m, Subject to the Parametric Restriction $k_1 = \Lambda = 0$

m	Yih[29]	Yacob et al.[30]	White[31]	Khan and Pop[24]	Present Study
0	0.4696	0.4696	0.4696	0.4696	0.4901
1/11	0.6550	0.6550	0.6550	0.6550	0.6623
1/5	0.8021	0.8021	0.8021	0.8021	0.8052
1/3	0.9276	0.9276	0.9277	0.9277	0.9292
1/2	–	–	1.0389	1.0389	1.0397
1		1.2326	1.2326	1.2326	1.2328

Table 4.2: A Comparative Assessment of $-\theta'(0)$ Across Varying m Values Under the Constraints $k_1 = \Lambda = N_b = N_t = 0$ and $Pr = 6$

m	Kuo[32]	Blasius[33]	Khan and Pop[24]	Present Study
0	0.8673	0.8673	0.8769	0.8771
1.0	1.1147	1.1152	1.1279	1.1276

In the present investigation, the dimensionless profiles of velocity, temperature, and concentration are examined under the influence of prescribed fluid-flow parameters. The analysis is carried out for selective parameter sets, namely. $k_1 = 0.1$, $m = 0.1$ & 0.4, λ = 0.1 & 0.5, $Pr = 1$ & 5, $Le = 1$ & 3, $N_b = 0.1$ & 0.5, $N_t = 0.1$, to elucidate the parametric sensitivity of the flow, heat, and mass transfer characteristics.

Figs:4.1-4.2 illustrate the shrinking and stretching velocity distribution for assorted k_1 with m. It is observed that the velocity exhibits a pronounced increase as $\boldsymbol{k_1}$ Rises for both $\boldsymbol{m} = 0.1$ & $\boldsymbol{m} = 0.4$, under prescribed flow conditions. Moreover, the momentum boundary layer thickness contracts noticeably when $\boldsymbol{m} = 0.1$ while for $\boldsymbol{m} = 0.4$, it shows a slight expansion before stabilizing. In both scenarios, the boundary layer ultimately attains an asymptotic state at a finite distance from the surface. This indicates that beyond a certain normal distance, momentum diffusion becomes negligible and the flow achieves a fully developed state, consistent with classical boundary-layer behaviour modified by elastico-viscous effects.

Figs. 4.3-4.4 illustrate the shrinking and stretching velocity distribution for assorted $\boldsymbol{m}$ with λ. The velocity exhibits an initial rise, yet as the parameter m intensifies, it undergoes a decline, and a further augmentation of λ amplifies this diminishing effect in both scenarios. Correspondingly, the momentum boundary layer thickness contracts sharply. This is due to the stronger wall shear and augmented viscous effects confining the momentum transport to a thinner region adjacent to the surface, yielding a steeper velocity gradient and a contracted boundary layer in both shrinking and stretching cases.

Figs:4.5-4.6 illustrate the shrinking and stretching velocity distribution for assorted λ with m. For the shrinking flow, the velocity weakens at $m = 0.1$ but intensifies at $m = 0.4$, whereas an opposite trend emerges in the stretching flow. In both situations, the velocity eventually stabilizes at the sheet surface. $\zeta = 5$. Moreover, the velocity boundary layer thickness expands noticeably for $m = 0.1$ but exhibits a slight contraction when $m = 0.4$, reflects the balance between nonlinear viscous effects and the imposed shrinking or stretching of the surface.

Figs:4.7-4.8 illustrate the shrinking and stretching temperature distribution for assorted λ with Pr. The temperature within the shrinking flow intensifies with the rise of λ, whereas in the stretching flow, the temperature exhibits a rapid decline for both $Pr = 1$ & $Pr = 5$. The Pr characterizes the relative transport rates of momentum and heat, being expressed as the ratio of momentum diffusivity to thermal diffusivity. For $Pr = 1$, the momentum and thermal diffusion processes proceed at comparable rates. However, when $Pr > 1$, momentum diffusion predominates over thermal diffusion, leading to a reduction in the thermal boundary layer thickness as the Pr increases. This phenomenon can be noticed in both cases.

Figs:4.9-4.10 illustrate the shrinking and stretching temperature distribution for assorted. $N_t\ with\ N_b$. For both cases, the fluid temperature rises with increasing. N_t at fixed values of $N_b = 0.1$ & $N_b = 0.5$. The thermal boundary layer exhibits a marked thickening under shrinking flow, whereas in the stretching flow, it undergoes a slight reduction in thickness. This contrasting behavior highlights the dominant role of flow kinematics in modulating nanoparticle-induced heat transfer mechanisms.

Figs:4.11-4.12 illustrate the shrinking and stretching concentration distribution for assorted. $N_t\ with\ N_b$. The concentration of the fluid declines markedly with increasing. N_t for both $N_b = 0.2$ & $N_b = 0.5$. Correspondingly, the concentration boundary layer thickness expands considerably with rising N_b at $N_b = 0.2$, while at $N_b = 0.5$, it contracts sharply as N_t increases in both scenarios. Increasing N_t consistently suppresses the concentration field due to stronger thermophoretic transport, whereas the influence of N_b governs whether the concentration boundary layer expands or contracts by modulating the balance between random diffusion and thermophoretic drift.

Figs:4.13 illustrate the concentration distribution for assorted. m with Le for the fixed wedge. The concentration boundary layer thickness diminishes with increasing. Le and m, signifying that within this layer, the dimensionless nanoparticle volume fraction attains comparatively higher values for the horizontal flat plate configuration. This explains the observed concentration distribution behavior for a fixed wedge, with more pronounced effects in the horizontal flat plate configuration.

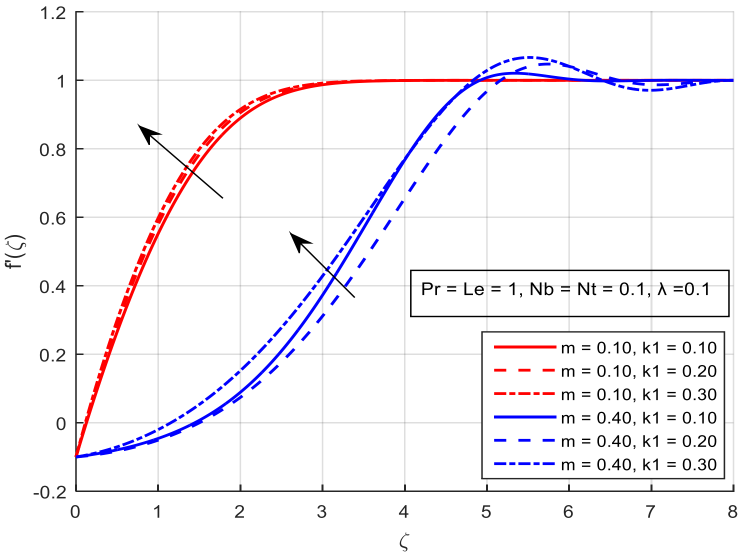

Fig. 4.1: Shrinking Velocity with k_1 and m.

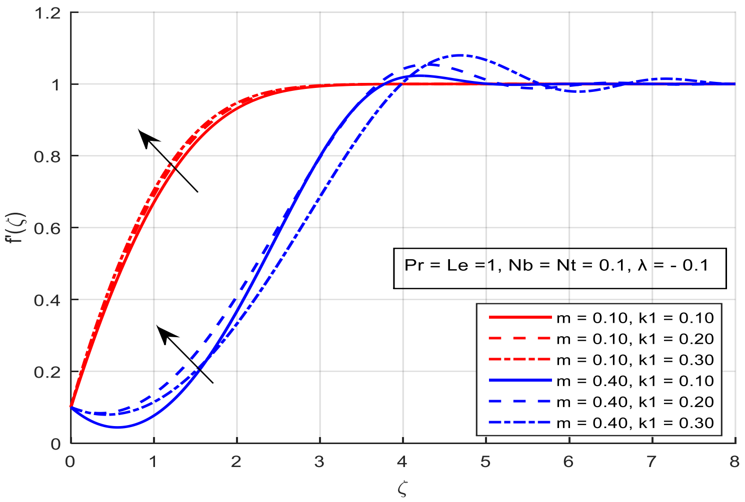

Fig. 4.2: Stretching Velocity with k_1 and m.

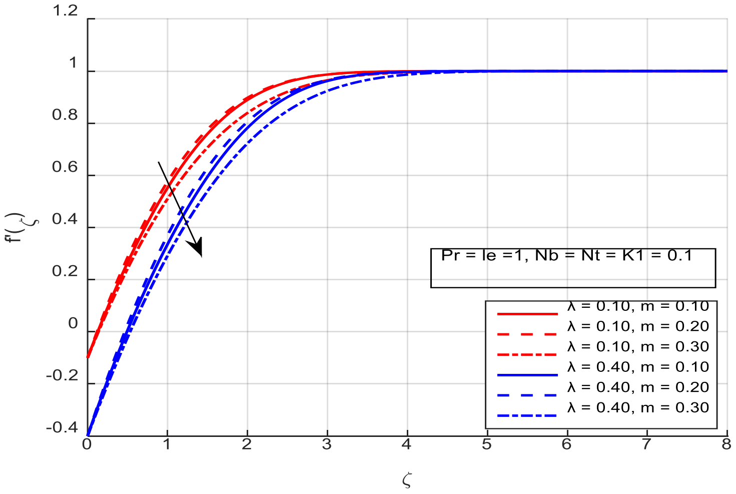

Fig. 4.3: Shrinking Velocity with m and $\boldsymbol{\lambda}$.

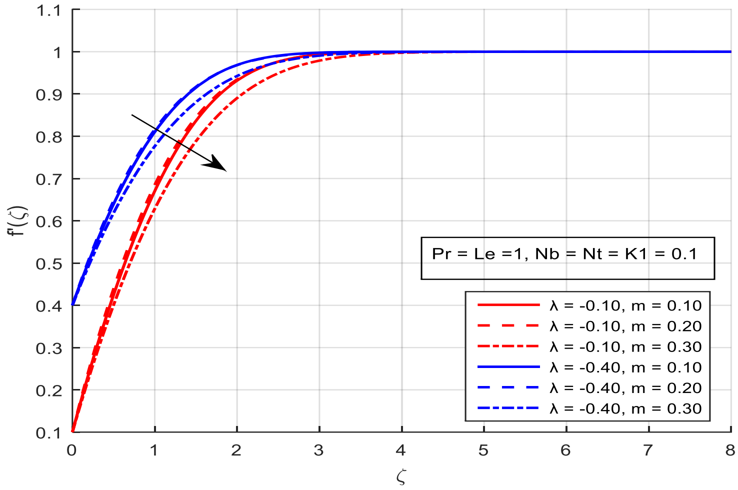

Fig. 4.4: Stretching Velocity with m and **λ.**

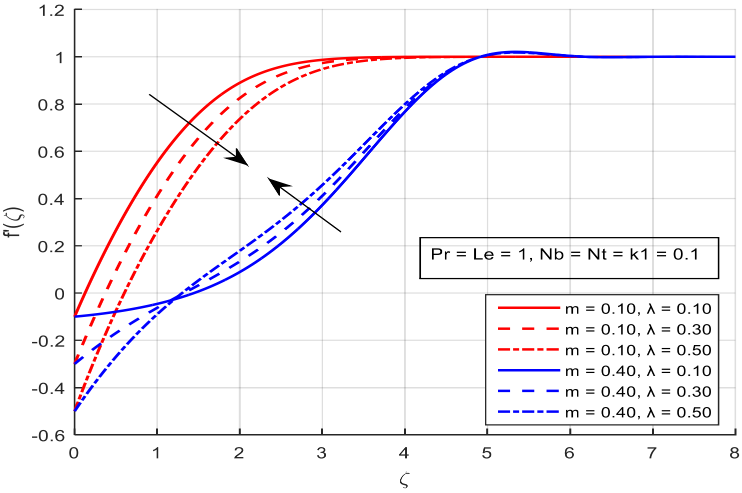

Fig. 4.5: Shrinking Velocity with **λ** and m.

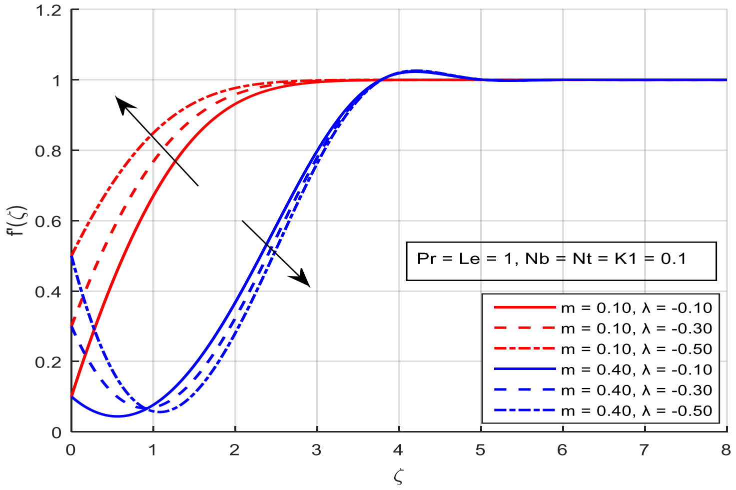

Fig. 4.6: Stretching Velocity with **λ** and m.

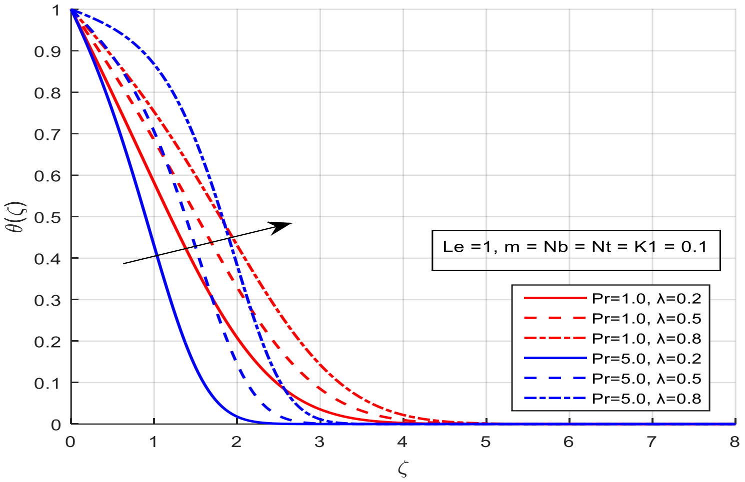

Fig. 4.7: Shrinking Temperature with $\boldsymbol{\lambda}$ and Pr.

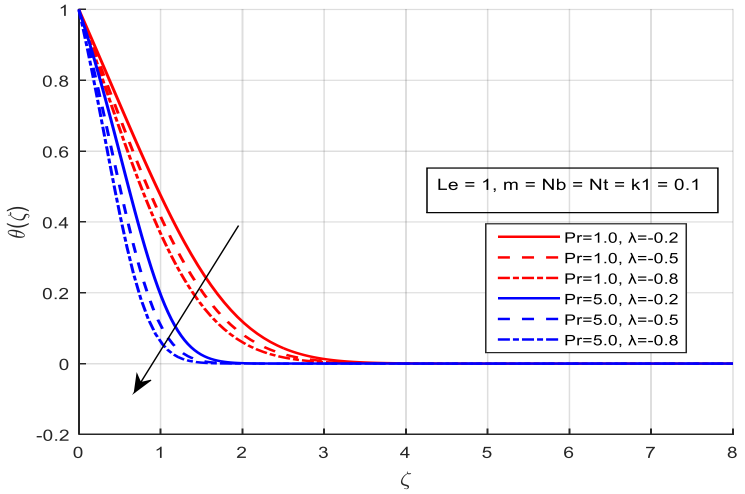

Fig. 4.8: Stretching Temperature with $\boldsymbol{\lambda}$ and Pr.

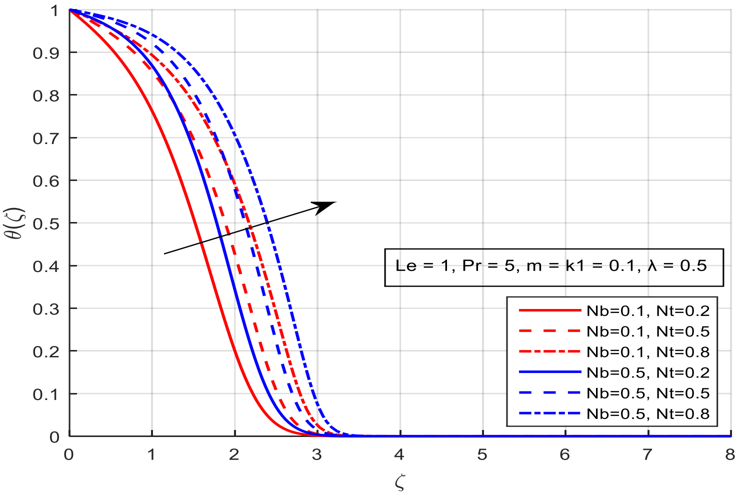

Fig. 4.9: Shrinking Temperature with $\boldsymbol{N_t}$ and $\boldsymbol{N_b}$.

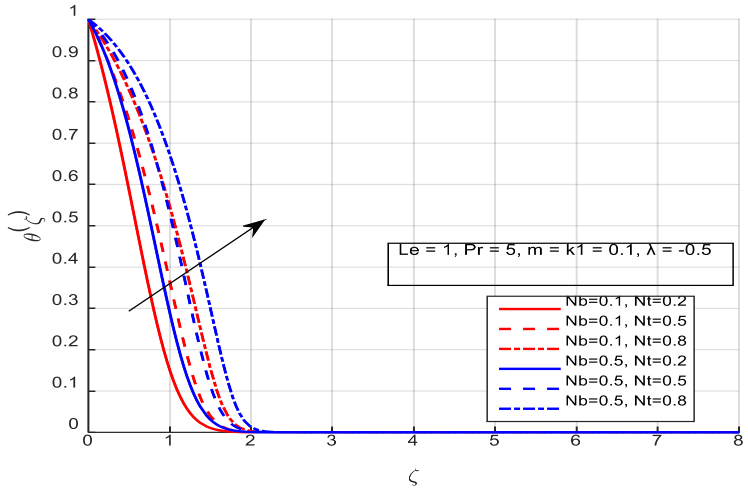

Fig. 4.10: Stretching Temperature with $\boldsymbol{N_t}$ and $\boldsymbol{N_b}$.

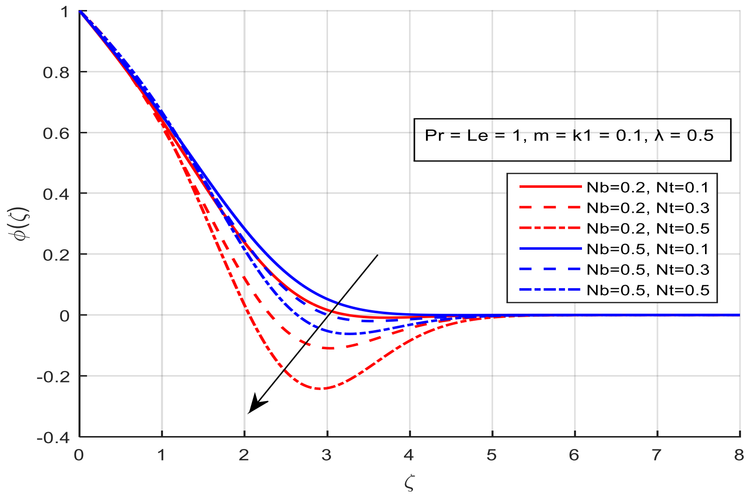

Fig. 4.11: Shrinking Concentration with $\boldsymbol{N_t}$and $\boldsymbol{N_b}$.

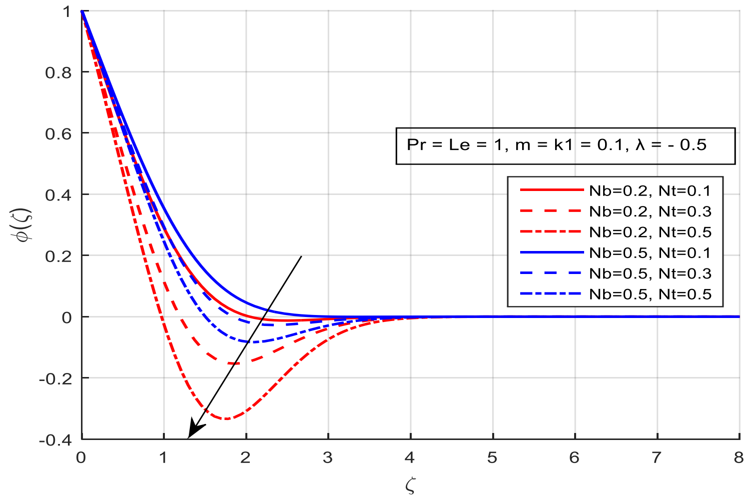

Fig. 4.12: Stretching Concentration with $\boldsymbol{N_t}$ and $\boldsymbol{N_b}$.

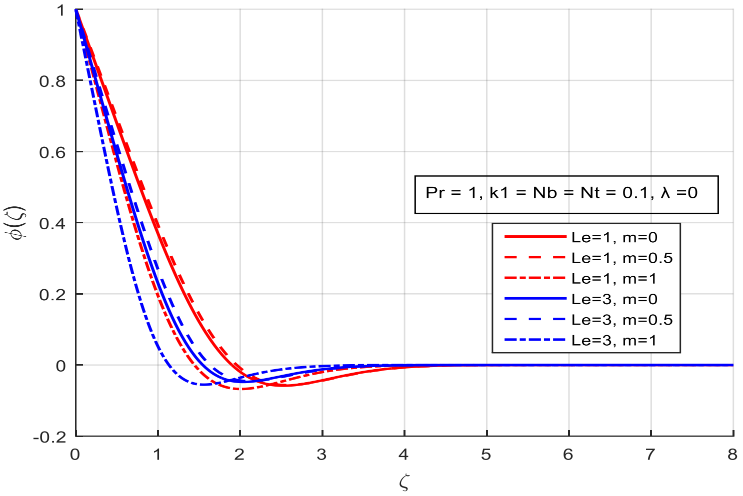

Fig. 4.13: Fixed Wedge Concentration with m and Le

5. Conclusion

The numerical exploration of the steady hydrodynamic boundary-layer configuration engendered by the motion of a wedge immersed in an aqueous nanofluid medium has been executed through the application of MATLAB's intrinsic boundary-value solver bvp4c across diverse parametric regimes characterized by m, k_1, A, λ, Pr, Le, N_b and N_t. The mathematical structure seamlessly collapses to the archetypal Falkner–Skan formulation of elastico-viscous (non-Newtonian) fluid flow past a stationary wedge when the slip-related and nanoparticle-induced modulating coefficients. k_1, λ, N_b and N_t asymptotically vanish. The ramifications of these dimensionless groups upon the velocity field, thermal distribution, and nanoparticle concentration profiles are meticulously delineated and exhibited in graphical form. Water-based nanofluids—engineered suspensions of nano-sized particulates such as Al_2O_3, TiO_2CuO, etc., or carbonaceous allotropes within a water matrix, are renowned for their amplified thermal transport capabilities. A further augmentation arises when such nanofluids are amalgamated with elastico-viscous bases, culminating in elastico-viscous nanofluids or hybrid nanofluids. These novel constructs exhibit pronounced heat-transfer enhancement, albeit concomitant with challenges encompassing elevated effective viscosity and possible colloidal instabilities.

The following are the main conclusions drawn from this research

- The velocity characteristics of both shrinking and stretching flows are strongly influenced by the governing parameters. An increase in k_1 augments the velocity profiles, whereas a rise in m leads to their attenuation. Interestingly, the shrinking velocity declines with the growth of λ, yet intensifies significantly with larger m; in contrast, the stretching velocity exhibits an opposite trend under the same parametric variations.
- The thermal behavior of the flow reveals contrasting trends; the shrinking temperature elevates while the stretching temperature diminishes with increasing λ under the influence of Pr. Conversely, for both shrinking and stretching cases, the temperature profiles intensify as N_t increases in the presence of N_b.
- The concentration in both shrinking and stretching flows exhibits a decline with the increase of N_t in the presence of N_b.
- The boundary layer dynamics reveal distinct behaviors under varying flow conditions. The momentum boundary layer consistently contracts in both shrinking and stretching cases, and the thermal boundary layer thickness either amplifies or attenuates with variations in Pr, while the concentration boundary layer exhibits rapid growth, it undergoes a marked reduction as N_b increases in both configurations.

Future Scope

Future investigations may extend elastico–viscous boundary layer flow over a wedge by incorporating hybrid or ternary nanofluids, variable thermos-physical properties, and non-Newtonian nanoparticle suspensions. The inclusion of thermal radiation, chemical reactions, Joule heating, and magnetic field modulation can enhance physical realism. Stability analysis, entropy generation, and validation through experiments or high-fidelity numerical simulations also offer promising directions.

References

[1] Falkner, V. M., & Skan, S. W. (1931). Some approximate solutions of the boundary-layer equations. *Philosophical Magazine*, *12*, 865–896. https://doi.org/10.1080/14786443109461870.

[2] Saidur, R., Kazi, S. N., Hossain, M. S., Rahman, M. M., & Mohamed, H. A. (2011). A review of the performance of nanoparticles suspended with refrigerants and lubricating oils in refrigeration systems. *Renewable and Sustainable Energy Reviews, 15*(1), 310–323. https://doi.org/10.1016/j.rser.2010.08.018.

[3] Mahian, O., Kianifar, A., Kalogirou, S. A., Pop, I., & Wongwises, S. (2013). A review of the applications of nanofluids in solar energy. *International Journal of Heat and Mass Transfer, 57*(2), 582–594. https://doi.org/10.1016/j.ijheatmasstransfer.2012.10.037.

[4] Behar, O., Khellaf, A., & Mohammedi, K. (2013). A review of studies on central receiver solar thermal power plants. *Renewable and Sustainable Energy Reviews, 23*, 12–39. https://doi.org/10.1016/j.rser.2013.02.017.

[5] Bondareva, N. S., Sheremet, M. A., Oztop, H. F., & Abu-Hamdeh, N. (2017). Heatline visualization of natural convection in a thick-walled open cavity filled with a nanofluid. *International Journal of Heat and Mass Transfer, 109*, 175–186. https://doi.org/10.1016/j.ijheatmasstransfer.2017.01.013.

[6] Saidur, R., Leong, K. Y., & Mohammad, H. A. (2011). A review on applications and challenges of nanofluids. *Renewable and Sustainable Energy Reviews, 15*, 1646–1668. https://doi.org/10.1016/j.rser.2010.11.035.

[7] Das, S. K., Choi, S. U. S., Yu, W., & Pradeep, T. (2008). *Nanofluids: Science and technology*. Hoboken, NJ: Wiley. https://doi.org/10.1002/9780470180693.

[8] Nield, D. A., & Bejan, A. (2013). *Convection in porous media* (4th ed.). New York, NY: Springer. https://doi.org/10.1007/978-1-4614-5541-7.

[9] Minkowycz, W. J., Sparrow, E. M., & Abraham, J. P. (2013). *Nanoparticle heat transfer and fluid flow* (Vol. IV). CRC Press, Taylor & Francis Group.

[10] Shenoy, A., Sheremet, M., & Pop, I. (2016). *Convective flow and heat transfer from wavy surfaces: Viscous fluids, porous media and nanofluids*. CRC Press, Taylor & Francis Group. https://doi.org/10.1201/9781315367637.

[11] Buongiorno, J., Venerus, D. C., Prabhat, N., McKrell, T., Townsend, J., Christianson, R., Tolmachev, Y. V., Keblinski, P., Hu, L., Alvarado, J. L., *et al.* (2009). A benchmark study on the thermal conductivity of nanofluids. *Journal of Applied Physics, 106*(9), 094312. https://doi.org/10.1063/1.3245330.

[12] Kakac, S., & Pramuanjaroenkij, A. (2009). Review of convective heat transfer enhancement with nanofluids. *International Journal of Heat and Mass Transfer, 52*(13–14), 3187–3196. https://doi.org/10.1016/j.ijheatmasstransfer.2009.02.006.

[13] Manca, O., Jaluria, Y., & Poulikakos, D. (2010). Heat transfer in nanofluids. *Advances in Mechanical Engineering, 2010*, 380826. https://doi.org/10.1155/2010/380826.

[14] Fan, J., & Wang, L. (2011). Review of heat conduction in nanofluids. *ASME Journal of Heat Transfer, 133*(4), 040801. https://doi.org/10.1115/1.4002633.

[15] Mahian, O., Kianifar, A., Kalogirou, S. A., Pop, I., & Wongwises, S. (2013). A review of the applications of nanofluids in solar energy. *International Journal of Heat and Mass Transfer, 57*(2), 582–594. https://doi.org/10.1016/j.ijheatmasstransfer.2012.10.037

[16] Sheikholeslami, M., & Ganji, D. D. (2016). Nanofluid convective heat transfer using semi-analytical and numerical approaches: A review. *Journal of the Taiwan Institute of Chemical Engineers, 65*, 43–77. https://doi.org/10.1016/j.jtice.2016.05.014.

[17] Myers, T. G., Ribera, H., & Cregan, V. (2017). Does mathematics contribute to the nanofluid debate? *International Journal of Heat and Mass Transfer, 111*, 279–288. https://doi.org/10.1016/j.ijheatmasstransfer.2017.03.118.

[18] Sheikholeslami, M., Mehryan, S. A. M., Shafee, A., & Sheremet, M. A. (2019). Variable magnetic forces impact on magnetizable hybrid nanofluid heat transfer through a circular cavity. *Journal of Molecular Liquids, 277*, 388–396. https://doi.org/10.1016/j.molliq.2018.12.104.

[19] Maatoug, S., Khan, S. U., Abbas, T., Ul Haq, E., Ghachem, K., Kolsi, L., *et al.* (2023). A lubricated stagnation point flow of nanofluid with heat and mass transfer phenomenon: Significance to hydraulic systems. *Journal of the Indian Chemical Society, 100*(6), 100825. https://doi.org/10.1016/j.jics.2022.100825

[20] Zhang, K., Li, Z., Wang, S., Wang, P., Zhang, Y., & Guo, X. (2023). Study on the cooling and lubrication mechanism of magnetic field-assisted Fe_3O_4@CNTs nanofluid in micro-textured tool cutting. *Journal of Manufacturing Processes, 85*, 556–568. https://doi.org/10.1016/j.jmapro.2022.11.081.

[21] Gupta, S. K. (2023). A short and updated review of nanofluids utilization in solar parabolic trough collector. *Materials Today: Proceedings.* https://doi.org/10.1016/j.matpr.2022.12.278.

[22] Hisham, S., Kadirgama, K., Alotaibi, J. G., Alajmi, A. E., Ramasamy, D., Sazali, N., *et al.* (2024). Enhancing stability and tribological applications using hybrid nanocellulose–copper (II) oxide (CNC–CuO) nanolubricant: An approach towards environmental sustainability. *Tribology International, 2024*, 109506. https://doi.org/10.1016/j.triboint.2024.109506

[23] Zawawi, N. N. M., Azmi, W. H., Hamisa, A. H., Hendrawati, T. Y., & Aminullah, A. R. M. (2024). Experimental investigation of air-conditioning electrical compressor using binary TiO_2–SiO_2 polyol-ester nanolubricants. *Case Studies in Thermal Engineering, 54*, 104045. https://doi.org/10.1016/j.csite.2024.104045.

[24] Khan, W. A., & Pop, I. (2013). Boundary layer flow past a wedge moving in a nanofluid. *Mathematical Problems in Engineering, 2013*, Article 637285. https://doi.org/10.1155/2013/637285.

[25] Nield, D. A., & Kuznetsov, A. V. (2011). The Cheng–Minkowycz problem for the double-diffusive natural convective boundary layer flow in a porous medium saturated by a nanofluid. *International Journal of Heat and Mass Transfer, 54*(1–3), 374–378. https://doi.org/10.1016/j.ijheatmasstransfer.2010.09.009.

[26] Kuznetsov, A. V., & Nield, D. A. (2010). Natural convective boundary-layer flow of a nanofluid past a vertical plate. *International Journal of Thermal Sciences, 49*(2), 243–247. https://doi.org/10.1016/j.ijthermalsci.2009.07.015.

[27] Kuznetsov, A. V., & Nield, D. A. (2006). Boundary layer treatment of forced convection over a wedge with an attached porous substrate. *Journal of Porous Media, 9*(7), 683–694. https://doi.org/10.1615/JPorMedia.v9.i7.20.

[28] Nield, D. A., & Kuznetsov, A. V. (2009). The Cheng–Minkowycz problem for natural convective boundary-layer flow in a porous medium saturated by a nanofluid. *International Journal of Heat and Mass Transfer, 52*(25–26), 5792–5795. https://doi.org/10.1016/j.ijheatmasstransfer.2009.07.024.

[29] Yih, K. A. (1998). Uniform suction/blowing effect on forced convection about a wedge: Uniform heat flux. *Acta Mechanica, 128*(3–4), 173–181. https://doi.org/10.1007/BF01182648.

[30] Yacob, N. A., Ishak, A., & Pop, I. (2011). Falkner–Skan problem for a static or moving wedge in nanofluids. *International Journal of Thermal Sciences, 50*(2), 133–139. https://doi.org/10.1016/j.ijthermalsci.2010.11.009

[31] White, F. M. (1991). *Viscous fluid flow* (2nd ed.). McGraw-Hill.

[32] Kuo, B. L. (2005). Heat transfer analysis for the Falkner–Skan wedge flow by the differential transformation method. *International Journal of Heat and Mass Transfer, 48*(23–24), 5036–5046. https://doi.org/10.1016/j.ijheatmasstransfer.2005.06.021.

[33] Blasius, H. (1908). Grenzschichten in Flüssigkeiten mit kleiner Reibung. *Zentralblatt für Mathematische Physik, 56*, 1–37.

Nomenclature

Greek Letters

β	Pressure-gradient index (N/m^{3})
λ	Wedge parameter (m)
$\boldsymbol{\upsilon}$	Kinematic viscosity ($\mathrm{m^2/s}$)
α	Thermal diffusivity ($\mathrm{m^2/s}$)
τ	Heat capacity ratio
ρ	Fluid density (Kg/m^{3})
$\boldsymbol{\psi}$	Stream function (Kg/(m.s))
ζ	Similarity variable
θ	Nanoparticles temperature fraction
$\emptyset$	Nanoparticles concentration fraction

m	Non-negative constant
Pr	Prandtl number
Le	Lewis number
N_b	Brownian diffusion coefficient (m/s)
N_t	Thermophoresis coefficient (m/s)

(u, v)	Velocity Component (m/s)
(x, y)	Cartesian Coordinate (m)
$u_w(x)$	Wedge surface velocity (m/s)
$u_e(x)$	External free stream velocity (m/s)
T	Temperature (K)
T_w	Surface temperature (K)
T_∞	Free-Stream temperature (K)
C	Concentration (mol/m^3)
C_w	Surface concentration (particles/m^2)
C_∞	Free Stream Concentration (mol/m^3)
k_0	Elastico-viscous parameter (Pa.s)
k_1	Modified elastico-viscous parameter (Pa.s)
D_B	Brownian diffusion coefficient (m^2/s)
D_T	Thermophoresis diffusion coefficient (m^2/s)
c	Volumetric heat capacity (J.$K^{-1}m^{-3}$)
ρ_p	Intrinsic density (m^{-3})
a	Non-negative constant
c	Non-negative constant
A	Pressure-gradient–related parameter (N/m^3)
ϕ_w	Concentration at the surface (Kg/m^3)
ϕ_∞	Concentration at the far-field (Kg/m^3)
$(\rho c)_p$	volumetric heat capacity at constant pressure (J/m^3K)
$(\rho c)_f$	volumetric heat capacity of the base fluid (J/m^3K)